Influence of lateral heterogeneities on strike-slip faults behavior: Insights from analogue models.

Sandra González-Muñoz[1], Guido Schreurs[2], Timothy C. Schmid[2], Fidel Martín-González[1]

[1]Área de Geología - ESCET, TECVOLRISK Research Group, Universidad Rey Juan Carlos. C/Tulipan s/n, Mostoles, 28933 Madrid, Spain
[2] Institute of Geological Sciences, University of Bern, Bern, Switzerland

Correspondence to: Sandra González Muñoz (sandra.gonzalezmu@urjc.es)

Abstract

This study investigates how lithological changes can affect the strike-slip faults propagation patterns using analogue models. Strike-slip fault zones are long structures that may cut across pre-existing tectonic or lithological steep boundaries. How strike-slip faulting is affected by a laterally heterogeneous upper crust is crucial for understanding the evolution of regional and local fault patterns, stress reorientations, and seismic hazard. Our models undergo sinistral distributed strike-slip shear (simple shear) and have been analyzed by Particle Image Velocimetry (PIV). We use quartz sand and microbeads as brittle analogue materials over a viscous mixture to distribute the deformation through the model. The first models investigate strike-slip faulting in a homogeneous upper crust by using quartz sand or microbeads only. Three further models examine how the presence of a central section which laterally differs in its properties, influences strike-slip faulting. The main observations are the following:

- The homogeneous upper crust shows typical Mohr-Coulomb strike-slip faults, with synthetic fault strikes related to the angle of internal friction of the material used

- The heterogeneity upper crust has a profound effect on synthetic fault propagation, interaction and linkage as well as the kinematic evolution of antithetic faults that rotate around a vertical axis.

- The orientation of the central section determines whether antithetic fault activity concentrates along the entire length of the central contact or not. In the first case, fault activity is segmented or the number of different faults formed is increased in distinct domains. In the second case, the

28   properties of the central material determines fault propagation, interaction and/or linkage across

29   the central domain.

30   •   These findings have potential implications for nature have been seen in the NW Iberian Peninsula.

31   In this area the change of direction of the sinistral faults and the position of the antithetic faults

32   can be explained due to lithological change.

Keywords

Strike-slip fault zone, Fault interaction, Fault linkage, Mechanical strength contrast, Analogue modelling

1. Introduction

Strike-slip fault systems in nature extend from a few meters to several hundred kilometers and typically

have complex geometries consisting of separate fault segments offset from each other or comprising

anastomosing, linked faults (e.g., Aydin and Nur, 1982; Barka and Kadinsky-Cade, 1988; Wesnousky,

1988; Stirling et al., 1996; Kim et al., 2004). The evolution of strike-slip fault systems has been studied

in numerous studies focused on the process of offset formation and therefore, basin development,

change of fault polarity and parameters controlling segmentation (e.g., Riedel, 1929; Anderson, 1951;

Deng et al., 1986; Sylvester, 1988; Dooley and Schreurs, 2012; Hatem et al., 2017; Lefevre et al.,

2020a; Visage et al., 2023). Understanding strike-slip fault interaction and linkage is important for its

implications on seismic hazard (Petersen et al., 2011; Bullock et al., 2014), in terms of dynamics, fault

growth and size of earthquakes (e.g. Aki, 1989; Harris and Day, 1999; Scholz, 2002; Wesnousky, 2006;

Shaw and Dieterich, 2007; de Joussineau and Aydin, 2009; Preuss et al., 2019); but also in terms of

regional stress orientations (Kirkland et al., 2008) and in view of the location of geothermal and

hydrocarbon resources (e.g. Sibson, 1985; Martel and Peterson, 1991; Aydin, 2000; Odling et al.,

2004; Cazarin et al., 2021).

How faults interact or link is considered to be a function of loading, stress disturbances, rheology and

the geometry of pre-existing structures (e.g., Kim et al., 2004; Myers and Aydin, 2004; Peacock and

Sanderson, 1991, 1992; Burgmann and Pollard, 1994; Sibson, 1985; Gamond, 1983; Rispoli, 1981;

Wesnousky, 1988). Various studies have investigated the influence of vertical changes in upper crustal

strength (e.g. a horizontal sedimentary sequence comprising layers or bodies of different strengths) on

strike-slip fault orientation, segmentation, linkage, and displacement. These studies used field observations, combined with analytical and numerical methods (e.g. Du and Aydin, 1995; Aydin and Berryman, 2010; De Dontney et al., 2011), or analogue models (Richard, 1991; Richard et al., 1995; Gomes et al., 2019; Gabrielsen et al., 2023; Venancio and Alves Da Silva, 2023). However, it is also important to consider the evolution of strike-slip fault systems in a laterally heterogeneous upper crust. Strike-slip faults often extend laterally over considerable distances and are thus expected to be influenced by steeply oriented pre-existing tectonic or lithological boundaries having rocks with contrasting strength on either side. Such (sub)vertical contacts often occur at terrane boundaries or within crustal blocks comprising rock units with contrasting strengths, e.g. a magmatic body with steep margins that intruded into a sedimentary sequence. To our knowledge no modelling studies have yet investigated how strike-slip fault systems are affected by steeply dipping contacts separating different rock types. Here we use scaled analogue model experiments analysed by Particle Imaging Velocimetry (PIV) to assess the role of vertically oriented domains of contrasting brittle strength in the upper crust on fault kinematics in distributed strike-slip shear. The models were inspired by the deformation pattern of the NW Iberian Peninsula, which has undergone sinistral shearing during the Alpine Orogeny (e.g. Martínez Catalán, 2011; Vergés et al., 2019). This particular area shows a system of sinistral faults that cross lithological domains with contrasting properties and part of their segmentation is conditioned by these domains.

2.   Methods

2.1.   Analogue model setup

The experimental set-up for simulating distributed strike-slip shear included a mobile base plate that could be translated horizontally above a fixed base plate (Fig. 1). An assemblage of 60 individual and moveable plexiglass bars (each 78 cm long, 5 cm high and 5 mm wide) was positioned on top of two base plates. The assemblage of plexiglass bars was confined by carbon-fiber sidewalls on the long sides (Fig. 1b) and wooden bars (c. 5 mm high, 2 cm wide and 40 cm long) on the short sides (Fig. 1b, c), that could pivot below the longitudinal sidewalls. The model was constructed on top of the plexiglass bars and consisted of a 2 cm-thick viscous layer, simulating the ductile lower crust, overlain by a 2 cm-thick layer of granular materials simulating the brittle upper crust. The short sides of the model were confined by vertical rubber

85 sheets. Although our model set-up included both a horizontal viscous layer overlain by a horizontal brittle

86 layer, our experiments focus on the influence of vertical domains with brittle strength contrasts on strike-

87 slip faulting. The function of the viscous layer, directly overlying the plexiglass bars, is to distribute the

88 applied shear deformation over the entire width of the model in the overlying brittle layer (e.g. Schreurs,

89 1991, 2003; Dooley and Schreurs, 2012).

90 Each model had an initial rectangular shape in map view, with a length of 78 cm parallel to the shear

91 direction and a width of 30 cm perpendicular to it. The movement of the mobile base plate occurred by

92 computer-controlled stepper motors at a constant velocity of 40 mm/h, resulting in 80 mm of total

93 displacement after two hours. Displacement of the mobile base plate changed the initial rectangular shape

94 of the overlying assemblage of plexiglass bars into a parallelogram simulating simple shear.

95
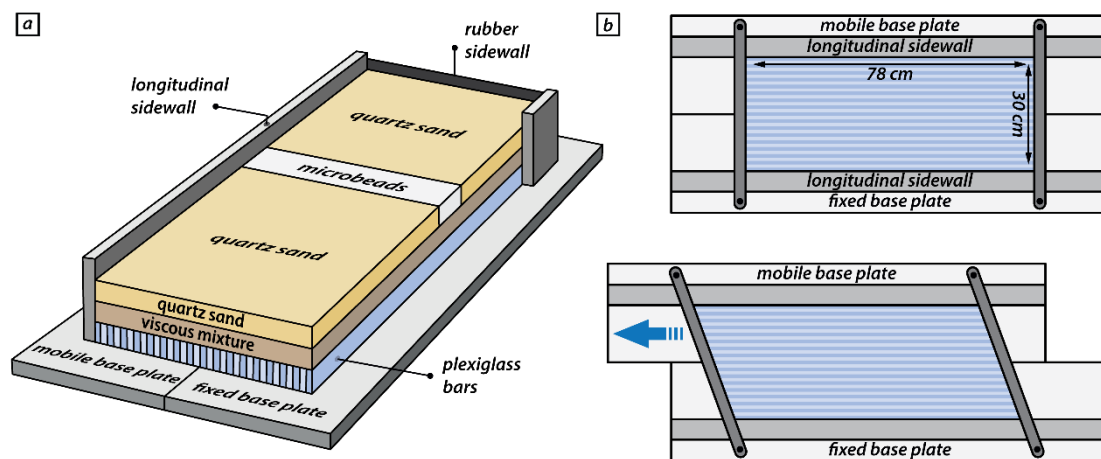
96

97 Figure 1: Schematic experimental setup. (a) The base of the model set-up consists of a fixed plate and a mobile
98 plate overlain by an assemblage of individual and moveable plexiglass bars. The model is constructed on top of
99 the plexiglass bars and is confined by two longitudinal sidewalls and two short sidewalls consisting of rubber
100 sheets. (b) upper panel: Initial position of base plates overlain by plexiglass bars confined on the short sides by
101 wooden bars that can pivot about a vertical axis; lower panel: Sinistral horizontal displacement of the mobile
102 base plate induces a simple shear movement in the overlying assemblage of plexiglass bars as they slide past one
103 another.

104

105 We performed four series of simple shear experiments, referred to as Series A, B, C and D (Fig. 2). Series

106 A involved two models with only one brittle material (Fig. 2a), quartz sand or microbeads, to investigate

107 strike-slip fault kinematics in a homogeneous upper crust, without any lateral variations in mechanical

108 strength. In the other three series (Fig. 2b-d), we introduced vertical domain boundaries across which the

109 mechanical strength varied laterally. Each model had three domains with a 5-cm-wide central domain

110 consisting of a different material than the domains on either side. The difference between Series B, C and

111 D is the orientation of the central domain with respect to the shear direction. To achieve such a model set-

112 up, two vertical thin sheets of cardboard (< 1 mm) were first placed as provisional walls, spaced 5 cm apart,

113 on top of the viscous layer in the central domain of the model, parallel to the required orientation of the

114 vertical domain boundaries. Subsequently, the different granular materials were sieved on top of the viscous

115 layer and once the desired model thickness was reached, the cardboard sheets were carefully removed.

116 Although removal of the cardboard produced increased dilation along a narrow zone, it hardly affects the

117 de facto function of this vertical boundary as a primary surface with materials of contrasting brittle strength

118 on either side. For descriptive purposes, we defined a North direction, which is perpendicular to the applied

119 shear direction and parallel to the short sides of the undeformed model (Fig. 2a). In models with a brittle

120 strength contrast, we can distinguish two outer domains, a western and an eastern one, and a central domain

121 (Fig. 2b-d).

122

123
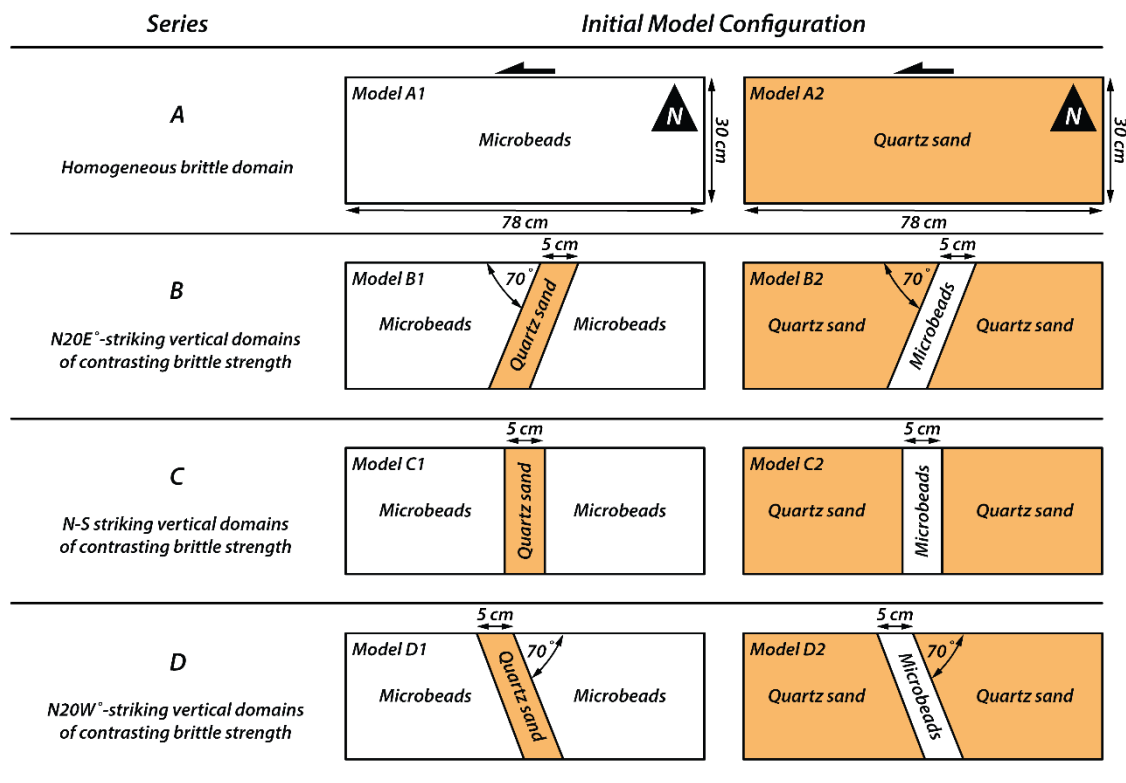
124 **Figure 2: Schematic drawing of the materials used and their surface distribution at the initial stage. All models**
125 **have a length of 78 and a width of 30 cm. The references about the patterns observed have been given by using**
126 **the long side of the edge of the models as "north". In the series of models referred as A, only one type of material**
127 **(quartz sand or microbeads) has been used. The diagrams of series B, C and D show the position and orientation**
128 **of the vertical domain boundaries in plan view and which materials were used.**

    2.2.   Analogue materials

130   We used two different types of granular materials in our analogue models to assess the role of vertical zones

131   of contrasting mechanical strength in the upper crust: quartz sand and microbeads grains. The quartz sand

132   (distributor Carlo Bernasconi AG; www.carloag.ch) has a grain size between 60 and 250 µm with a bulk

133   density of 1560 kg m^{-3}, whereas the grain size of the microbeads (distributor: Worf Glasskugeln, Germany)

134   lies between 150 and 210 µm with a bulk density of 1400 kg m^{-3}. These density values were achieved by

135   sieving the granular material into the model box from a height of 30 cm. Both, quartz sand and microbeads

136   deform according to the Coulomb failure criterion and have internal peak friction angles of 36° and 22° and

137   cohesion values of 50 ± 26 Pa and 25 ± 4 Pa, respectively (Panien et al., 2016; Schmid et al., 2020). The

138   considerable difference in the internal peak friction angle between the two materials makes them suitable

139   for simulating contrasting upper crustal rocks. According to their difference in the internal friction angle,

140   we consider the microbeads and quartz sand as weak and strong materials, respectively.

141   The viscous layer in our models had a density of 1600 kgm^{-3} and consisted of a mixture of SGM-36

142   polydimethylsiloxane (PDMS) and corundum sand (weight ratio of 0.965: 1.000). The mixture has a quasi-

143   linear viscosity of 1.5×10^5 Pa s and a stress exponent of 1.05 (Zwaan et al., 2018). The properties of all

144   analogue materials are summarized in Table 1.

145

146

Granular materials	Quartz sand	Microbeads	Viscous material	PDMS/corundum mixture
Density (kg/m^3)	1560	1400	Density (kg/m^3)	1600
Grain size (µm)	60-250	150-210	Viscosity (Pa s)	1.5×10^5
Peak friction coefficient µ and angle, ϕ	0.72 - 36°	0.41 - 22°	Stress exponent n	1.05
Cohesion (Pa)	50 ± 26	25 ± 4		

147   **Table 1:** Materials properties of used granular and viscous materials (after Panien et al., 2006; Schmid et al., 2020).
148

    2.3.   Scaling

150   For brittle Mohr-Coulomb type materials, dynamic similarity is given by the equation for stress ratios

$$\sigma^* = \rho^* g^* h^* \tag{1},$$

151   where ρ^*, g^* and h^* are the ratios of model to nature for density, gravity and length, respectively. Note,

152   that our two used granular materials have different densities, cohesions and internal friction coefficients.

153   However, the resulting scaling factors are nearly identical and therefore we provide only the scaling factors

154   for quartz sand. Where scaling factors substantially differ, we denote them with subscripts "qtz" and "mb"

155   for quartz sand and microbeads, respectively. Our model setup yields a length scaling factor of $h^* =$

156   2×10^{-6} and a gravity scaling factor of 1. For quartz sand, the density scaling factor is $\rho^*_{qtz} \sim 0.6$ and the

157   cohesion factor is $C^*_{qtz} = 1 \times 10^{-6}$ (using a cohesion of ~50 Pa and 50 MPa for our quartz sand and upper

158   crustal rocks, respectively; Byerlee, 1978). Additionally, for microbeads the density scaling factor and

159   cohesion scaling factor are $\rho^*_{mb} \sim 0.5$ and $C^*_{mb} = 1 \times 10^{-6}$ (assuming a weakened natural rock type with a

160   cohesion of c. 25 MPa), respectively. Using these scaling factors yields a stress scaling factor of $\sigma^* =$

161   1×10^{-6} for both quartz sand and microbeads.

162   Assuming a lower crustal viscosity of $\eta = 10^{22}$ Pa s (Moore and Parsons, 2015; Zhang and Sagiya, 2017)

163   yields a viscosity ratio $\eta^* = 1 * 10^{-17}$ (using the viscosity of $1.5 * 10^5$ Pa s for the viscous analogue

164   material).

165   The strain rate ratio is obtained from the stress ratio and the viscosity ratio by (Weijermars and Schmeling,

166   1986):

$$\dot{\varepsilon}^* = \frac{\sigma^*}{\eta^*} \tag{2}.$$

167   Note that due to the simple shear setup, we substitute the strain rate scaling factor $\dot{\varepsilon}^*$ with the shear strain

168   rate scaling factor $\dot{\gamma}^* = 1 \times 10^{11}$. Next, the velocity scaling factor v^* and a time scaling factor t^* are

169   calculated with

$$\dot{\gamma}^* = \frac{v^*}{h^*} = \frac{1}{t^*} \qquad (3)$$

170   yielding a velocity scaling factor $v^* = 2 \times 10^5$ and a time scaling factor $t^* = 1 \times 10^{-11}$.

171   Based on our scaling, 1 cm in our experiments corresponds to 5 km in nature and the applied velocity of 40

172   mm h^{-1} converts to a velocity of ~2 mm a^{-1} in nature. Using the shear strain rate scaling factor $\dot{\gamma}^*$, the bulk

173   shear strain rate $\dot{\gamma} = 3.7 \times 10^{-5}\ s^{-1}$ in our models translates to a shear strain rate of $\dot{\gamma} = 3.7 \times 10^{-16}\ s^{-1}$

174   in nature and 1 h in our analogue experiments translates to ~12.5 Myr in nature.

175   In order to verify dynamic similarity of brittle natural and experimental material we calculate the

176   Smoluchowski number S_m, which is the ratio between gravitational stress and cohesive strength (Ramberg,

177   1981):

$$S_m = \frac{\rho g h}{C + \mu \rho g h} \qquad (4),$$

178   where ρ, h, C and μ are the density, thickness, cohesion, and friction coefficient, respectively of the brittle

179   material. With a cohesion of 50 MPa and a friction coefficient of ~0.6 (Byerlee, 1978) for upper crustal

180   rocks, this yields values of $S_m \sim 1$ for our models as well as for nature. We further calculate the Ramberg

181   number R_m to ensure dynamic and kinematic similarities between the viscous layers.

$$R_m = \frac{\rho g h^2}{\eta v} \qquad (5)$$

182   For our velocity of 40 mm h^{-1}, this yields a Ramberg number of 6 for both, our models and nature. The

183   Reynolds number R_e is defined as the ratio between inertial forces and viscous forces and is for all our

184   models as well as for the natural prototype $\ll 1$:

$$R_e = \frac{\rho v h}{\eta} \qquad (6)$$

185   Based on the applied scaling laws, the material properties and the similar non-dimensional numbers for

186   model and nature, we consider our models to be properly dynamically scaled. Model parameters and

187   dynamic numbers of the used materials are specified in Table 2.

188

	General parameters			Brittle upper crust		Ductile lower crust		Dimensionless numbers		
	Gravity [m/s^2]	Crustal thickness [m]	Shear velocity [m/s]	Density [kg/m^3]	Cohesion [Pa]	Density [kg/m^3]	Viscosity [Pa s]	Smoluchowski Sm	Ramberg Rm[1]	Reynolds Re
Model	9.81	4 x 10^{-2}	1.1 x 10^{-6}	1560	50	1600	1.5 x 10^5	1	6	<<1
Nature	9.81	2 x 10^4	6.3 x 10^{-11}	2700	5 x 10^7	2900	1 x 10^{22}	1	6	<<1

Scaling ratios x* = x^m/x^n [dimensionless]								
σ^*	ρ^*	g^*	h^*	C^*	$\dot{\gamma}^*$	η^*	v^*	t^*
1 x 10^{-6}	0.5^1-0.6	1	2 x 10^{-6}	5^1-10 x 10^{-7}	1 x 10^{11}	1 x 10^{-17}	2 x 10^5	1 x 10^{-11}

189   [1] Lower values for scaling factors ρ^* and C^* refer to microbeads.

190   **Table 2:** Scaling parameters and scaling factors.
191

192
193
194   **2.4.**   **Deformation monitoring and quantification**

195   Since the experiments were conducted using a simple shear setup, vertical motions during deformation

196   were negligible, with nearly all movement located within the horizontal plane. The different experiments

197   were monitored by an automated Nikon D810 (36 MPx) DSLR camera positioned above the experimental

198   model. Images were taken at fixed intervals of 60 s during two hours, resulting in 121 subsequent top view

199   images of the model surface. For a quantitative 2D analysis of the surface deformation, we used the

200   StrainMaster module of the LaVision© DaVis image correlation software. Using a calibration plate, the

201   software corrects the top view images for lens distortion effects (i.e., unwarping), applies image

202   rectification and provides a scaling function that maps coordinates from the camera sensor to physical

203   coordinates with a resolution of ~9 px/mm. The digital image correlation calculates local displacement

204   vectors on subsequent images using a square matching algorithm with adaptive multi-pass cross-

205   correlation. To properly track the grain movement patterns, we sprinkled coffee grains on the model surface

206   prior to the model run. For each image, the analyzed area is subdivided into small interrogation window for

207   which a local displacement vector is determined by cross-correlation. We used subsets (i.e., interrogation

208   windows) of 31 by 31 pixels with a 75% overlap for the local displacement calculations that, assembled

209   result in incremental (60 s interval) displacement fields for the horizontal x- and y-components u_x and u_y,

210   respectively with a vector resolution of ~1.3 vectors/mm.

211   Postprocessing included an outlier filter to fill gaps of pixels within a 3 by 3 neighborhood (Westerweel

212   and Scarano, 2005). Discarded vectors in the displacement fields were replaced by an iterative interpolation

213   requiring at least two neighboring vectors. For quantifying deformation at the model surface, we calculate

214   the z-vorticity ω_z (i.e., a rotation measure in the xy plane) as a proxy for shear movement along strike-slip

215   faults. In our models the X-axis corresponds to the long side of the rectangle; and the Y-axis corresponds

216   to the short side of the model. In contrast to the shear strain ε_{xy}, vorticity is not dependent on the orientation

217   of the coordinate system, which is crucial when quantifying deformation along faults that strike obliquely

218   with respect to the coordinate system (e.g., Cooke et al., 2020). ω_z can be derived from local displacement

219   gradients according to equation 1:

$$\omega_z = \frac{\partial u_y}{\partial x} - \frac{\partial u_x}{\partial y} \tag{7}$$

220   With u_x and u_y being the horizontal displacement components in the x, and y direction, respectively. Positive

221   and negative ω_z values refer to sinistral and dextral relative displacement, respectively. Within the

222   predefined increment of 60 s, ω_z values are consistently within the range [-2%, 2%] and we set a threshold

223   of -0.5% and 0.5% to distinguish between active deformation and background noise for dextral and sinistral

224   shear sense, respectively. In the results section we present ω_z at deformation stages every 30 min (i.e., after

225   30, 60, 90, and 120 min). Finite deformation after 120 min for each model is illustrated with a surface

226   photograph and enhanced with superposed line drawings of the fault pattern. For the statistical analysis of

227   fault orientations, we traced active fault segments (i.e., $\omega_z \leq$ -0.5 % or $\omega_z \geq$ 0.5 %) in MATLAB using

228   polylines, where each fault segment is defined by two consecutive vertices. At each time step, segment

229   length and azimuth were calculated and visualized in length-weighted rose diagrams.

230

231

232

3. Results

3.1. Series A: Fault evolution in a homogeneous upper crust

The Series A models consisted of a homogeneous upper crustal layer composed of either microbeads (Fig. 3; Model A1) or quartz sand (Fig. 3; Model A2). The incremental strain panels document that strain localized first in the model with quartz sand, while deformation was still diffuse in the model with microbeads (Fig. 3a and f), i.e. strain localization occurs at lower amounts of applied simple shear in quartz sand than in microbeads. With progressive sinistral simple shear deformation, slightly overlapping right-stepping *en echelon* strike-slip faults with a sinistral displacement formed (Fig. 3b and g). These faults were synthetic with respect to the bulk simple shear. In the model with microbeads (Model A1) the first synthetic faults had an orientation of N79˚E (Fig. 3b), whereas in the model with quartz sand (Model A2) their orientation was N72˚E (Fig. 3g). Initial deformation in both models is accommodated by synthetic (sinistral) strike-slip faults (Fig. 3a, b and f, g). As deformation progressed, individual fault segments linked up forming major sinistral strike-slip faults (Fig 3c and h). Antithetic faults only developed in Model A2 (quartz sand only; Fig. 3h and i) at later stages of deformation. These faults were confined in between previously formed synthetic faults. The final deformation stage (Fig. 3e and j) shows that most deformation was taken up by major synthetic faults that crossed the entire length of the model. At the final stage, the initial *en echelon* pattern of faulting was better preserved in the quartz sand model than in the microbeads model, resulting in a wider damage zone in the former.

252
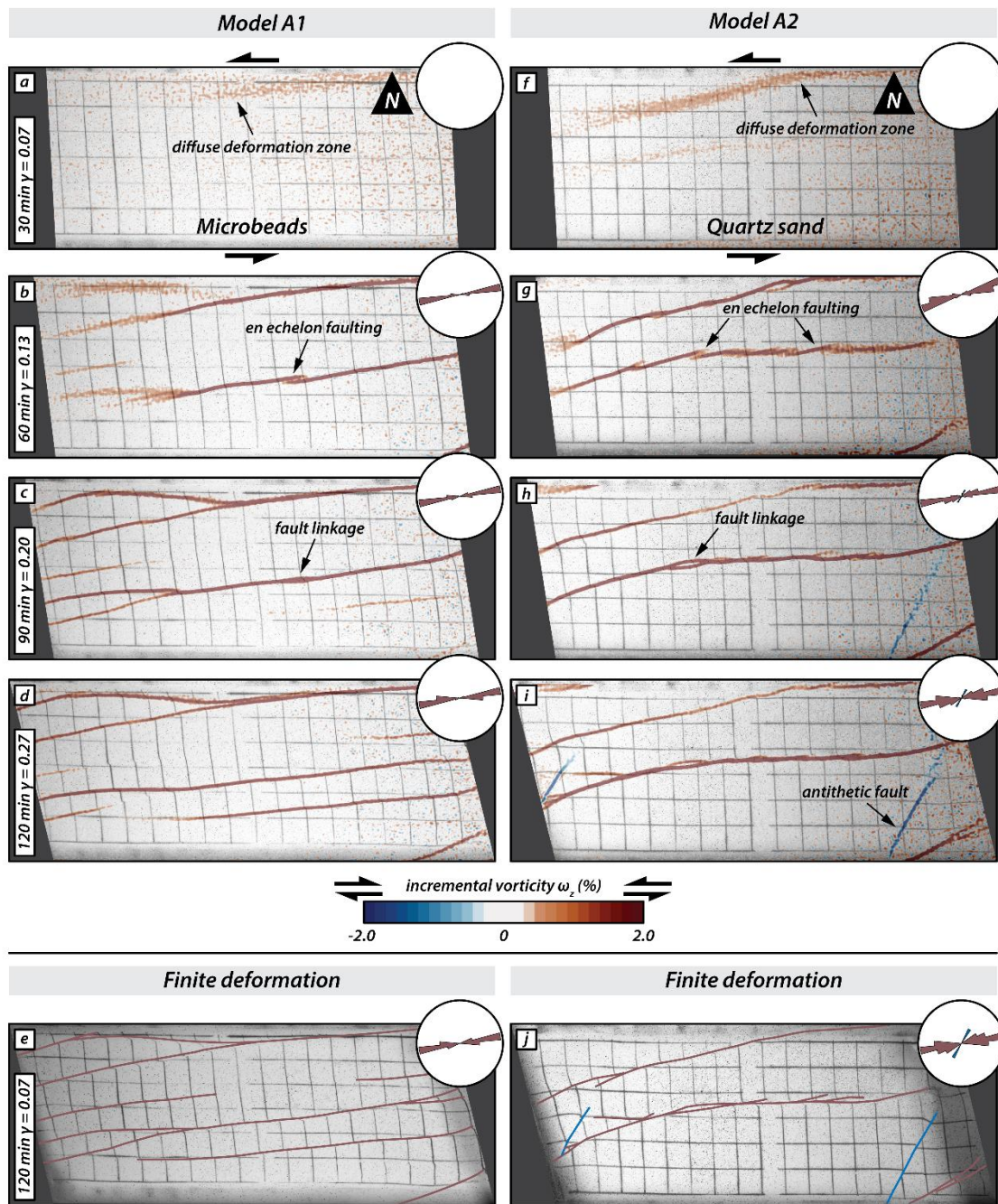
Figure 3: Overview of Series A models: Simple shear deformation of two models with a homogenous upper brittle layer. The first four panels of each series show surface photographs with the incremental vorticity after 30 minutes (20 mm displacement of mobile base plate), 60 minutes (or 40 mm displacement), 90 minutes (or 60 mm displacement) and 120 minutes (or 80 mm displacement). Incremental positive and negative values indicate sinistral (synthetic, red) and dextral (antithetic, blue) relative movement, respectively. The last panel for each series shows a surface photograph of the final stage overlain with the interpreted fault pattern; red lines are sinistral faults, blue lines are dextral faults.

253
254
255
256
257
258
259

260

261

262

3.2. Series B: Fault evolution in models with N20°E vertical domain boundaries

The vertical domain boundaries in the Series B models were oriented N20°E. Model B1 had a central domain consisting of strong quartz sand with weak microbeads in the adjacent, western and eastern domains (Fig. 4; Model B1), whereas in Model B2 it was the other way around. (Fig. 4; Model B2). Both models showed the development of dextral strike-slip (antithetic, with respect to sinistral simple shearing) faults along the vertical boundaries of the central domain (Fig. 4a, f). Later, sinistral strike-slip faults (synthetic) formed in the western and eastern domains (4b, g). Although these faults propagated laterally with time, none of the synthetic faults crossed the central domain. Instead, they halted at or close to the boundary faults along the central domain (Fig. 4c, h). In Model B1 a few antithetic faults formed in between pre-existing synthetic faults in the western and eastern domains, striking at c. N60°E (Fig. 4d, e). Antithetic faults developed also in the western and eastern domains of Model B2, almost coevally with the synthetic faults. They strike at higher angles to the shear direction than those antithetic faults confined between overlapping synthetic faults in Model B2. With increasing deformation, the central domain and its bordering antithetic faults rotated counterclockwise in both models (Fig. 4a-e, f-j), as did the antithetic faults in the western and eastern domains, which acquired a slight sigmoidal shape form (e.g. Fig. 4j)

278
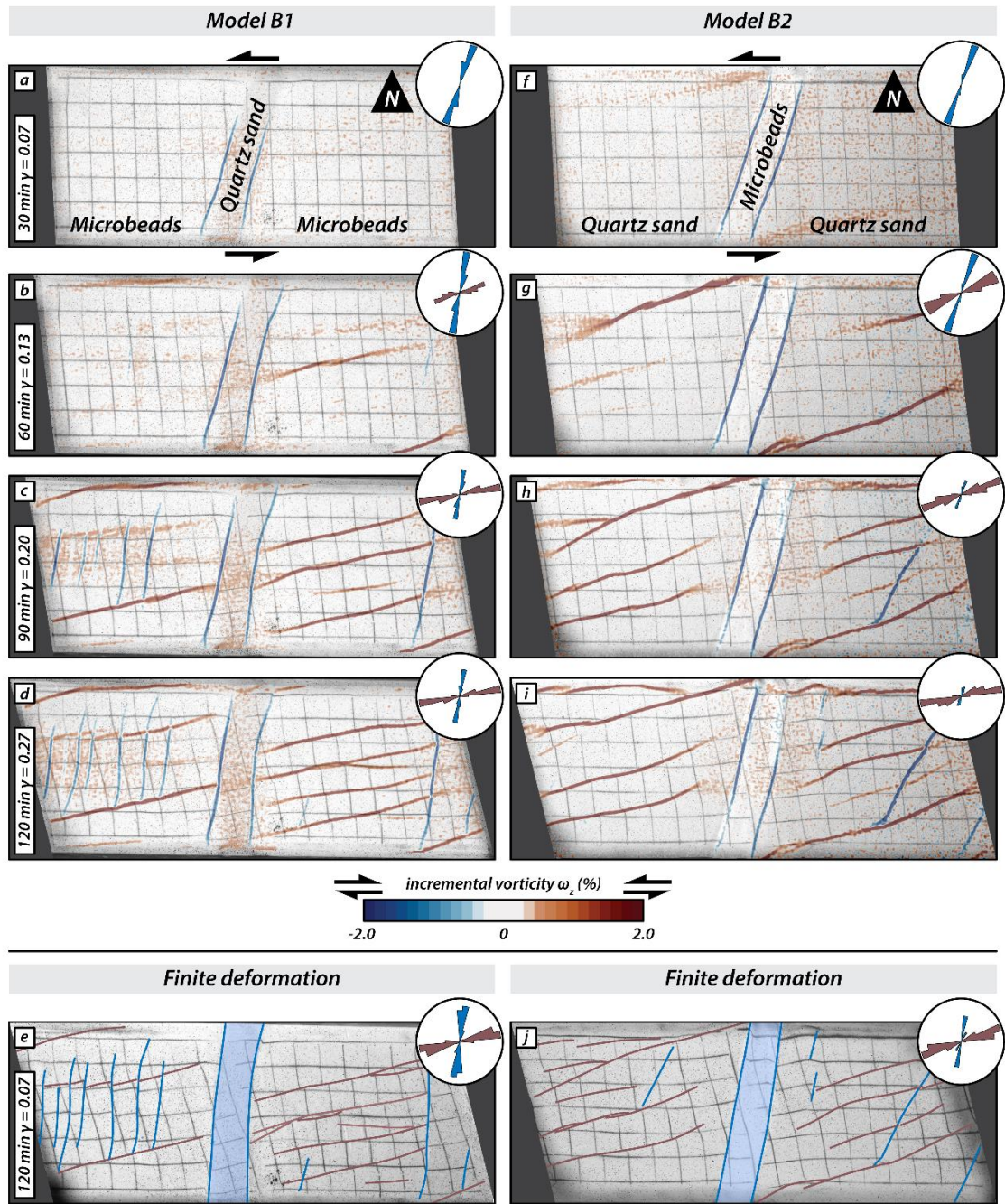
Figure 4: Overview of Series B models: Simple shear deformation of two models with vertical domains of contrasting brittle strength oriented N20°E. The first four panels of each series show surface photographs with the incremental vorticty after 30 minutes (20 mm displacement of mobile base plate), 60 minutes (or 40 mm displacement), 90 minutes (or 60 mm displacement) and 120 minutes (or 80 mm displacement). Incremental positive and negative values indicate sinistral (synthetic, red) and dextral (antithetic, blue) relative movement, respectively. The last panel for each series shows a surface photograph of the final stage overlain with the interpreted fault pattern; red lines are sinistral faults, blue lines are dextral faults.

286

287

288

289

3.3. Series C: Fault evolution in models with N-S vertical domain boundaries

290

291 During the early stages of simple shear, dextral (antithetic) faults formed along the N-S striking borders of

292 the central domain (Fig. 5b, g) in both models, but earlier and more pronounced in Model C1. With

293 progressive shearing, both synthetic and antithetic faults formed in the outer domains of both models (Fig.

294 5c and h). In Model C2, activity along the antithetic faults bordering the central domain ceased, and

295 synthetic faults propagated from the outer domains into the central weak domain (Fig. 5h-j). In contrast, in

296 Model C1, the antithetic faults along the borders of the central domain remained active, and no synthetic

297 faults crossed the central strong domain (Fig. 5d). In the eastern domain of Model C2, a few antithetic faults

298 formed in between major synthetic faults, striking at a lower angle to the shear direction than earlier formed

299 antithetic faults in the western domain. With progressive simple shear the central domain showed

300 counterclockwise rotation around a vertical axis in both models and antithetic faults obtained a sigmoidal

301 shape in top view (Fig. 5i). As the initial N-S antithetic faults bordering the central domain rotated

302 counterclockwise, activity along these faults stopped and new fault segments parallel to earlier antithetic

303 faults formed in the western and eastern domains (Fig. 5d, e). At the final stage of Model C2, antithetic

304 faults dominated in the western domain and synthetic faults in the eastern domain. In contrast, in Model

305 C1, antithetic and synthetic faults were present in both the western and eastern domain.

306
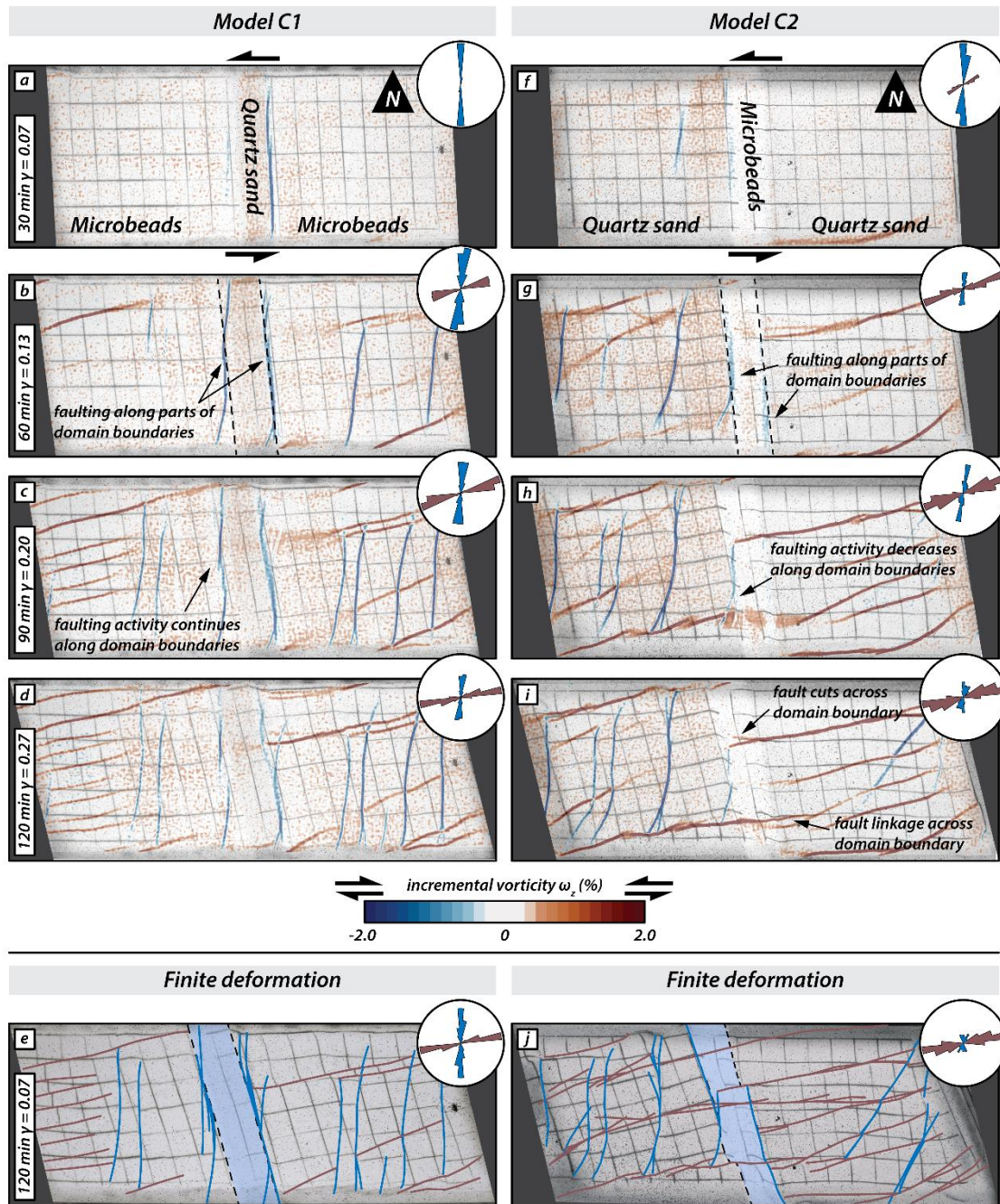
Figure 5: Overview of Series C models: Simple shear deformation of two models with vertical domains of contrasting brittle strength striking N-S. The first four panels of each series show surface photographs with the incremental vorticty after 30 minutes (equivalent to 20 mm displacement of the mobile base plate), 60 minutes (or 40 mm displacement), 90 minutes (or 60 mm displacement) and 120 minutes (or 80 mm displacement). Incremental positive and negative values indicate sinistral (synthetic, red) and dextral (antithetic, blue) relative movement, respectively. The last panel for each series shows a surface photograph of the final stage overlain by the interpreted fault pattern; red lines are sinistral faults, blue lines are dextral faults.

314

315

3.4. **Series D: Fault evolution in models with N20°W striking vertical domain boundaries**

In contrast to the Model C series, no faults formed along the boundaries of the central domain in both Models D1 and D2 (Fig. 6a and f). Model D1 is dominated by synthetic faults crosscutting the central strong domain (6c-e). As these faults traversed the central domain, they slightly changed their strike. In contrast, in Model D2 the weak microbeads of the central domain were internally deformed and oblique-slip reverse faults formed, which propagated laterally and parallel to the domain boundaries (Fig. 6g-j). Synthetic faults formed both in the western and eastern domain of Model D2, while antithetic faults formed later and in between overlapping synthetic faults (Fig. 6g-j). With progressive deformation synthetic faults from the western and eastern domain in Model D2 propagated partially into the central, weak central domain, but halted at the previously formed oblique-slip reverse faults (Fig. 6h and i). During late stages of deformation a few antithetic faults formed in Model D1 in between earlier formed synthetic faults, striking at larger angles to the shear direction than in Model D2.

328
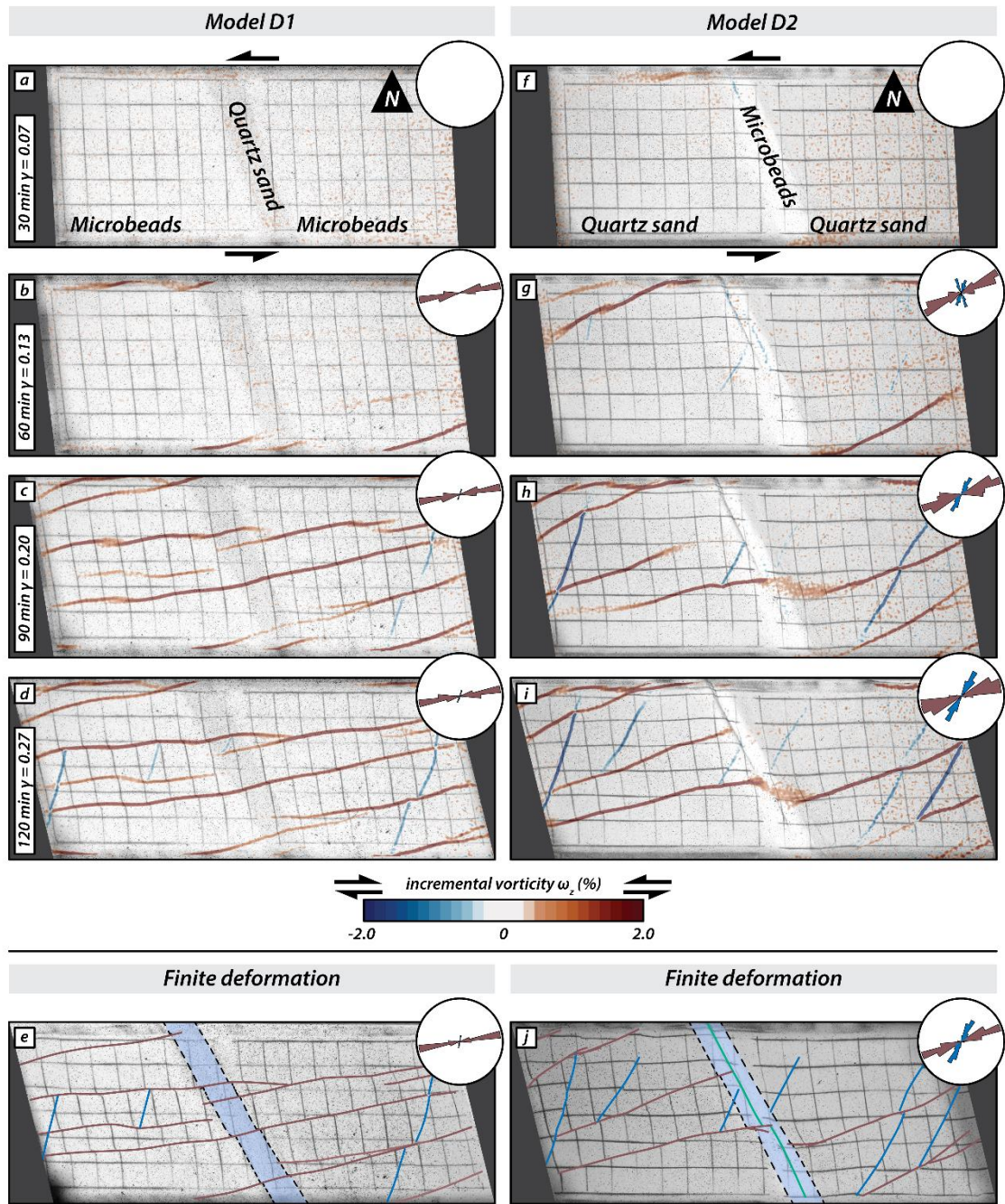
Figure 6: Overview of Series D models: Simple shear deformation of two models with N20°W striking vertical domains of contrasting brittle strength. The first four panels of each series show surface photographs with the incremental vorticty after 30 minutes (20 mm displacement of mobile base plate), 60 minutes (or 40 mm displacement), 90 minutes (or 60 mm displacement) and 120 minutes (or 80 mm displacement). Incremental positive and negative values indicate sinistral (synthetic, red) and dextral (antithetic, blue) relative movement, respectively. The last panel for each series shows a surface photograph of the final stage overlain with the interpreted fault pattern; red lines are sinistral faults, blue lines are dextral faults, green line indicates reverse fault.

337

338

339

4. Discussion

4.1. Series A: Strike-slip faulting in models with a homogeneous upper crust model

In our models simulating homogeneous crust the structures display an *en echelon* pattern, as should be expected (Bartlett et al., 1981; Sylvester, 1988; Misra et al., 2009). Initial bulk simple shear is accommodated in both models by zones of diffuse deformation and is followed by localized deformation along narrow fault zones. It is interesting to note that localization requires a higher shear deformation in the model with the weak material than in the model with strong material. This difference in localization behaviour is attributed to the difference in dilatancy between the two analogue materials, which is closely related to grain shape and grain size distribution. The weak material, represented by the microbeads, are well-rounded and have a narrow grain size distribution (150-210 μm), whereas the strong material (quartz sand grains) is angular and have a wider grain size distribution (60-250 μm). The more uniform the grain shape and grain size, the more applied shear deformation is needed to localize the strain along a narrow fault zone (Antonellini et al., 1995; Mair et al., 2002). Therefore, the shape and grain-size characteristics will influence the time that a fault may take to reactivate depending on the lithology that comprises its fault zone (e.g. Sammis et al., 1987; Mair et al., 2002).

In these two models sinistral (synthetic) strike-slip faults form first. The initial strike of these faults differs between the model with the weaker material and the one with strong material, striking at N79°E and N72°E, respectively. The internal friction angle of each type of material will be adjusted to a certain orientation of rupture according to the Mohr-Coulomb criterion. (Fig. 7). At the beginning of the experiment, the main principal stress (σ_1) is oriented at 45° to the shear direction, and the two potential fault orientations strike at 45° - $\phi/2$ and at 45° + ϕ /2 to σ_1, respectively with ϕ the angle of internal peak friction, which is 22° for the microbeads and 36° for quartz sand (Fig. 7). Hence, the synthetic and antithetic faults strike at N79°E and N11°E, respectively in the model with microbeads and at N72°E and N18°E in the model with quartz sand respectively. The fact that nearly all deformation is accommodated by synthetic faults is typical of simple shear models with an initial rectangular shape, i.e. a large aspect ratio of length (parallel to shear direction) divided by width (Schreurs, 2003; Dooley & Schreurs, 2012). A comparison of previous simple shear experiments shows that the shape of the initial model has an influence on the relative proportion of synthetic and antithetic faults (Gapais et al., 1991; Schreurs, 2003). With decreasing aspect ratio, the number of antithetic faults will increase, and in case of an initially square-shaped model, (i.e., aspect ratio

369   is 1) antithetic faults will dominate (Gapais et all., 1991; Dooley & Schreurs, 2012). In the model with

370   quartz sand, a few antithetic faults form in between previously formed major synthetic faults (Fig. 3i).

371   These late antithetic faults, however, form in response to local stress field modifications between

372   overlapping synthetic faults, causing σ_1 to rotate clockwise from 45° to the bulk shear direction towards an

373   orientation that is subparallel to the previously formed synthetic faults. As a consequence, these late

374   antithetic faults are not in the "conjugate" position with respect to the synthetic major faults, but strike at

375   lower angles with respect to the long borders of the model (these are the lower-angle antithetic faults of

376   Schreurs, 2003).
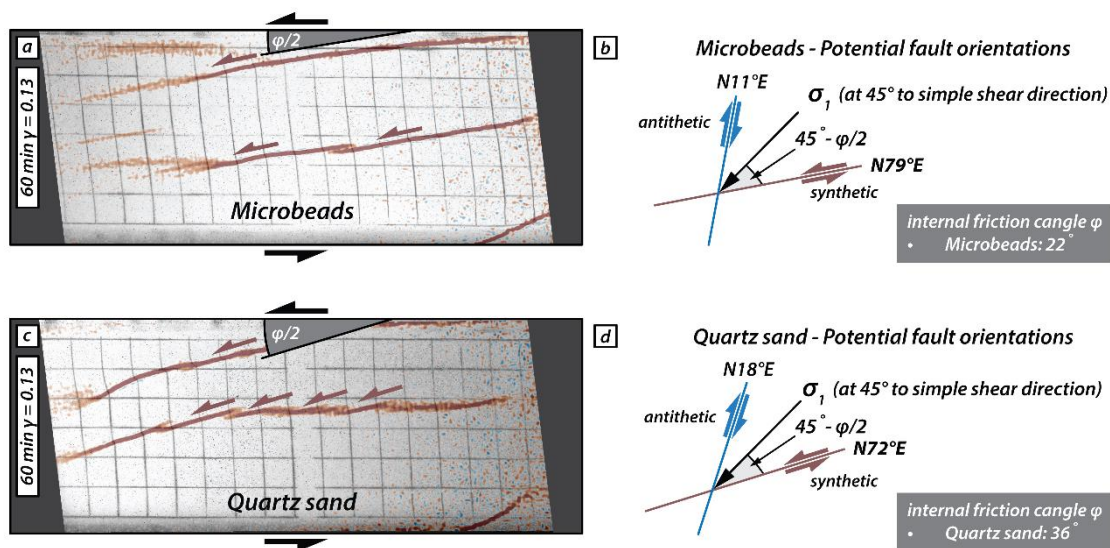
377
378   **Figure 7: Illustrative scheme of the expected fault orientation according to the Mohr-Coulomb failure criteria,**
379   **for the experiments with only one type of material (homogeneous upper crust). a) and c) Surface photographs**
380   **of the model with microbeads only (a) and quartz sand only (c), with the incremental vorticty after 60 minutes**
381   **(40 mm displacement). b) and d) Schematic explanation for the expected orientation of the synthetic and**
382   **antithetic faults considering the simple shear orientation along with the Mohr-Coulomb failure criteria, for the**
383   **models with microbeads and quartz sand only respectively.**

384

385   ## 4.2.   Series B, C and D: The influence of the orientation lateral heterogeneities on strike-slip

386   faulting

387   Introducing a vertical domain with different properties that the surrounding material results in different

388   fault patterns and timing of the structures (Segall and Pollard, 1983; Peacock, 1991; Peacock and

389   Sanderson, 1992; Schellart and Strak, 2016; Lefevre et al., 2020; Livio et a., 2019;Venancio and Alves Da

390   Silva, 2023). The degree of difference in the fault pattern is a function of the orientation and the strength

391   of the domains.

- Vertical domain boundaries activated
- No faults cross-cutting central domain
- Three structurally distinct domains
- Syn- and antithetic faults in W and E, slightly sigmoidal shape in surface view

- Vertical domain boundaries activated
- No faults cross-cutting central domain
- Three structurally distinct domains
- Synthetic faults dominate; antithetic faults form in between major synthetic faults due to local stress field modifications

- Vertical domain boundaries activated along most of their length
- Faults along central domain become sigmoidal at their northern and southern ends
- Three structurally distinct domains
- Syn- and antithetic faults in W and E, with antithetic faults having a slightly sigmoidal shape in surface view

- Vertical domain boundaries partially activated; activity decreases with progressive shearing and counterclockwise rotation of central domain
- Initially three structurally distinct domains
- With progressive shearing, synthetic faults cross-cut central domain
- Syn- and antithetic faults in W and E, slightly sigmoidal shape in surface view

- Vertical domain boundaries not activated
- Faults cross-cut central domain
- No distinct domains
- Synthetic faults dominate
- Antithetic faults are confined between major synthetic faults and form due to local stress field modifications

- Internal deformation within weak central domain results in oblique-slip dextral reverse faults, creating a stress barrier
- Faults propagate laterally into weak domain, but halt against previously formed oblique-slip reverse faults
- With increasing shear, strike-slip faults most likely will link up across central domain
- Antithetic faults are confined between major synthetic faults and form due to local stress field modifications

Figure 8: Schematic surface views summarizing the main results from the models with vertical domains of contrasting brittle strength.

396   The first thing noticed is that the faults do not follow the *en echelon* pattern and the antithetic faults are the

397   first one to be form (Figs. 4 and 5). The domain boundaries in Series B and C models initially strike N20°E

398   and N-S respectively (Fig. 8a, b, c and d), which is close to the antithetic fault orientation predicted by the

399   Mohr-Coulomb failure criterion (i.e. N11°E for microbeads and N18°E for quartz sand, see section 4.1).

400   As a result, the domain boundaries in both models are activated along their entire length, and the antithetic

401   faults are formed along the borders of the central domains (Fig. 8a, b and c). With progressive sinistral

402   simple shear, the central domain bounded by the fault rotates counterclockwise about a vertical axis and, at

403   the end of the experiment has rotated about 12° striking N08°E. The faults of the domain boundaries remain

404   active throughout the model run, because their strike is favorably oriented respect the main stress (Fig 8a,

405   b). As a result the sinistral faults in the series B and in model C1 cannot propagate along the entire model,

406   regardless of the composition of the central domain, and two possibilities are shown: the faults are

407   segmented (Fig 8a and b) or more new faults are generated in the eastern and western domains (Fig. 8c).

408   However, if the central domain is composed of the weak material and is not fully surrounded by antithetical

409   faults, the synthetic fault can crosscut the entire model (Fig. 8d). This may offer the possibility that strike-

410   slip fault stepping may also be due to the action of lithology, which is able to induce fault segmentation.

411   Hence, the presence laterally heterogeneous upper crust with steep boundaries and suitable oriented for

412   activation by antithetic faults, can prevent the synthetic strike-slip faults from crossing certain domains.

413   The antithetic faults that form in the outer domains of our models are of two types: (i) those that form

414   relatively early in as yet largely unfaulted domains and strike at large angles to the shear direction (Fig. 8a,

415   c and d) and (ii) those confined between earlier formed and overlapping synthetic faults that strike at lower

416   angles to the shear direction (Fig. 8b, e and f). In the first case, the early-formed antithetic faults reflect the

417   orientation predicted by the Mohr-Coulomb failure criterion; striking N18°E if the outer domains consist

418   of the strong material and N11°E if the outer domains consist of the weak material. Due to lateral fault

419   propagation and coeval rotation of the central fault segments, these antithetic faults obtain a slightly

420   sigmoidal shape form in map view during progressive simple shear (see also Schreurs, 1994, 2003; Dooley

421   and Schreurs, 2012). In th second case, the antithetic faults confined in between closely spaced, earlier

422   formed, synthetic faults have an initial different strike (N15°-N20°E in the weak material, e.g. Model C1)

423   and N25°- N30°E in the strong material, (e.g. Model C2). The antithetic faults confined between major

424   synthetic faults result from local stress field modifications governed by relative movement of material in

425   between previously formed synthetic faults with large overlap (Schreurs, 2003; Dooley and Schreurs, 2012;

426   their R'$_L$ faults). Both types of antithetic faults rotate counterclockwise with progressive sinistral simple

427   shear. Rotation of faults and blocks in strike-slip fault systems is not only observed in analogue models

428   (Schreurs, 1994, 2003; Dooley and Schreurs, 2012), but has also been documented in nature (e.g., Ron et

429   al., 1986; Nicholson et al., 1986). It is thus important to keep in mind that antithetic faults (and blocks in

430   between) can undergo considerable rotation about a vertical axis during simple shear deformation, implying

431   that present-day antithetic fault orientations in strike-slip fault systems do not necessarily reflect the

432   orientations in which they initially formed.

433   In comparison with the Series B and Series C models, the initial N20°W striking central domain boundaries

434   in the Series D models are the least favorably oriented for antithetical fault activation. Consequently, the

435   fault development pattern follows an echelon type, but in both cases the size of the segments is affected by

436   the lateral variation of the material properties. In the weak-strong-weak Model D1 (Fig. 8e and f), the

437   domain boundaries are not activated at all and the synthetic faults forming in the outer domains propagate

438   across the central domain. Apart from a slight re-orientation of the fault strike, reflecting the difference in

439   material strength between central and outer domains (difference in internal friction angles), the fault pattern

440   in Model D1 is similar to the one in Model A1, which had no vertical brittle strength contrasts. The strong-

441   weak-strong Model D2 shows a different deformation behaviour. Although the domain boundaries at the

442   surface are not activated, the presence of a weak material surrounded by strong material results in internal

443   deformation within the central domain and dextral oblique-slip reverse faults form striking parallel to the

444   domain boundaries. These faults prevent synthetic faults from crossing the central domain, and they halt

445   against the oblique-slip reverse faults.

446

447   **4.3.   Fault linkage across central domain**

448   In models where synthetic faults from the eastern and western domain cross-cut the central domain, the

449   entire model behaves as one domain. As shown in the section above, this is the case for models C2, D1,

450   and D2 where the vertical boundaries of the central domain are not or only partially activated, depending

451   on the orientation of the central domain (section 4.2). However, all three models show distinct differences

452   in how laterally propagating synthetic strike-slip faults link across the central domain (Fig. 9). For model

453   D1 (Fig. 9a, b), faults cross-cut the stronger central domain from the eastern and western domains (Fig. 9a)

454   linking up in a new segment. This new segment shows different orientation resulting in a step-like linkage

455   pattern in surface view (i.e., flat-steep-flat; Fig. 9a, b). When segmentation occurs and the faults cross the

456   central domain, the orientation of the faults is different, probably related to the internal friction angles

457   between the quartz sand and the microbeads (Du and Aydin, 1995; de Doney et al., 2011).

458
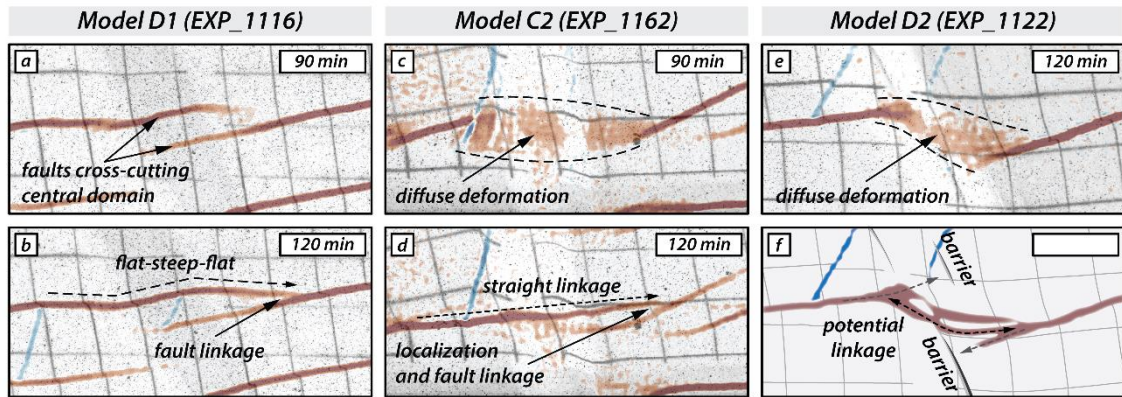
Figure 9: Surface detailed photographs of the central domain of the models with the contrasting brittle mechanical strength, showing the fault linkage across the central domain at 90 minutes (60 mm displacement) and 120 minutes (80 mm displacement). a) and b) model D1 with the central domain striking N20˚W and composed by the strong material (quartz). c) and d) model C2 with the central domain striking N-S and composed by the weak material (microbeads). e) model D2 with the central domain striking N20˚W and composed by the weak material (microbeads). f) Schematic drawing for the fault linkage at the last stage.

465

466   For models C2 and D2, however, the domain configuration strong-weak-strong has implications for fault

467   linkage. As synthetic strike-slip faults propagate from the western and eastern domains towards the weaker

468   central domain, early deformation patterns are characterized by a zone of diffuse deformation across the

469   central domain (Fig. 9c, e). In model C2, the fault from the W domain cross-cuts the weak central domain

470   and eventually links with the fault in the E domain in a straight fashion after 120 min (Fig. 9d), abandoning

471   earlier active fault strands striking N18°E (i.e., the predicted orientation for Mohr-Coulomb failure

472   criterion). Similar fault kinematics should be expected for model D2 (Fig. 9e, f). However, laterally

473   propagating faults in the western and eastern domain do not link during the duration of the model run.

474   Instead, the two fault segments halt at the domain boundary resulting in ongoing diffuse deformation

475   without strain localization in the central domain. This behavior may be explained by the presence of the

476   N20°W-striking reverse faults within the central model domain. Due to the misalignment between central

477   domain boundaries and the expected orientation of antithetic faults, the domain boundaries do not activate

478   and domain-internal deformation is taken up by oblique-slip dextral reverse faults. Such faults (i.e., nearly

479   orthogonally striking with respect to synthetic faults) accommodate bulk shear deformation hindering the

480 synthetic faults to propagate. In that sense, the oblique-slip reverse faults act as an impenetrable barrier

481 inhibiting linkage of synthetic faults across the weak central domain (Fig. 9f). Oblique-slip reverse faults

482 in the central domain, therefore, influence fault interaction across the central domain in a similar way as do

483 the activated domain boundaries in models B1, B2, and C1 (Fig. 8).

484

485 ### 4.4.   Comparison with strike-slip fault zones in Iberia

486 The NW Iberian Peninsula contains major sinistral and dextral strike-slip intraplate fault systems (Fig. 10a).

487 These intraplate fault systems are located in an old basement developed during Variscan Orogeny

488 (Devonian-Carboniferous, e.g., Matte, 1991; Martínez Catalán et al., 1997; Fernández et al., 2004), during

489 this stage a set of lithologic units with contrasting properties such as granites, quartzites, slates and high-

490 grade metamorphic rocks were emplaced and deformed. During the Alpine Compression (Late Cretaceous

491 to the present), the present fault pattern was obtained due to the collision between the Iberian microplate

492 and the northern edge of Africa in the middle Miocene (e. g., Alonso et al., 1996; Vegas et al., 2004; Martín-

493 González and Heredia, 2011, Martín-González et al., 2012). This collision caused the Iberian Peninsula to

494 undergo a counterclockwise twist, resulting in slight shearing (e.g. Martínez Catalán, 2011; Vergés et al.,

495 2019). In the study area, intraplate deformation led to a fault pattern primarily composed of sinistral faults,

496 such as the Penacova-Régua-Verin (PRVF), Manteigas-Vilariça-Bragança (MVBF), and Orense faults (see

497 Fig. 10a). Additionally, antithetic dextral faults were also generated (see Fig. 10a).
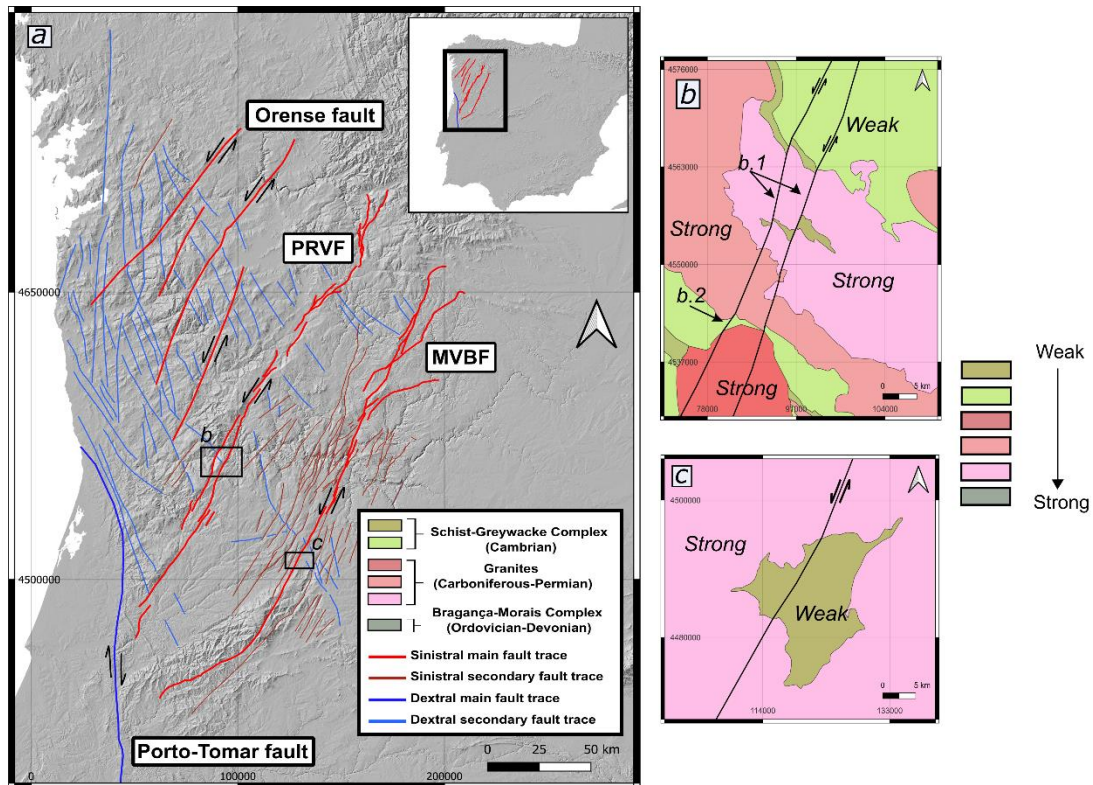
Figure 10: a) Digital elevation model of the northwest section of the Iberian Peninsula where the main faults are drawn, with the location of Figures b and c. The faults are essentially sinistral and there is a dextral fault on the southern edge that delimits the study area. In blue and light red, the secondary antithetic (dextral) and synthetic (sinistral) faults have been marked respectively. b) Schematic representation of the southern section of the Verin fault showing patterns of directional changes similar to models D1 and D2. c) Schematic representation of the southern section of the Vilariça fault showing a similar deformation pattern to model C2.

Among the traces of these faults, we can observe antithetic faults that do not connect with each other and, in some cases, acquire a sigmoidal as observed in Models C1 and C2 models (Fig. 8e and f). These antithetic faults are not in a conjugate position and mostly confined between major sinistral faults. At the end of the sinistral faults is the Porto-Tomar fault, which delimits the study area. The Porto-Tomar fault shows dextral displacement and tectonically delimits the area to the north and south of Portugal (Veludo et al., 2017). The main traces of the sinistral faults are not completely straight, but show slight changes in strike. For example, along the PRVF, the fault undergoes a counterclockwise refraction when crossing from weak into strong lithologies (b.1 in Fig. 10b), similar to Model D1 with strong quartz sand in the central domain (Fig. 10b). On the other hand, the same fault undergoes a clockwise refraction as it crosses from strong lithologies (granites) in shaly units (b.2 in Fig. 10b), similar to Model D2 with weak microbeads in the central domain. The same phenomenon is also observed along the Vilariça fault when the fault intersects granites and slate units (Fig. 10c).

518   Although on a local scale, similarities are observed in the behaviour of individual faults crossing contrasting

519   lithologies in nature and faults crossing vertical domain boundaries in our analogue models, the NW Iberian

520   Peninsula strike-slip fault system as a whole does show little resemblance with the overall fault patterns in

521   homogeneous or laterally heterogeneous upper crustal models. This may indicate that the NW Iberian crust

522   is much more heterogeneous and complex than the one modelled in our experiments.

523

5.   Conclusions

525   We performed a series of analogue models to investigate faulting in the upper, brittle crust as a result of

526   sinistral simple shear. In a first series of models, the upper crust was homogeneous and consisted of a single

527   analogue material, either weak microbeads or strong quartz sand. In three further series of models, the upper

528   crust is laterally heterogeneous and consisted of three domains with vertical boundaries and contrasting

529   strength (i.e. a weak-strong-weak or a strong-weak-strong configuration).

530   - The fault pattern in a homogeneous upper crust is dominated by sinistral (synthetic) strike-slip faulting,

531   whose orientations are readily explained by the Mohr-Coulomb failure criterion, with fault strikes

532   being a function of the internal friction angles. In models with heterogeneous upper crust, the

533   development of the faults does not follow an *en echelon* pattern. The sinistral faults are developed in

534   the outer domains, in the expected orientations according to the Mohr-Coulomb failure criterion.

535   - The heterogeneity of the upper crust, as lateral variations of the lithology, could affect the expected

536   sequence of strike-slip faults with antithetic faults being the first to form. If the initial strike of the

537   boundaries of the domains is subparallel to the predicted Mohr-Coulomb, the development of antithetic

538   faults is promoted. As a consequence, faulting may occur in distinct structural domains and faults may

539   be segmented. If the orientation is less favorable, the development of antithetic faults is not promoted,

540   allowing synthetic faults to form without distinct structural domains.

541   - The properties of the lithology that intersect the sinistral faults, influences how their segments are

542   connected. In the case of weak-strong-weak, the synthetic faults from the outer domains cross-cut the

543   central domain with a slight change in strike orientation, whereas in the case of strong-weak-strong,

544   the weak central domain show internal oblique-slip reverse faulting, which inhibits faults from the

545   outer domain to fully cross the central domain.

546   -   Although we only tested sinistral simple shear, our results can also be applied to dextral simple shear

547   by mirroring the fault patterns around a N-S axis.

548   -   There are similarities between the behaviour of individual faults in natural systems and our

549   heterogeneous upper crustal models, i.e. the slight change in strike orientation when crossing a

550   boundary with contrasting strength.

551

6. Competing interests

553 The contact author has declared that none of the authors has any competing interests.

7. Acknowledgments

555 The following work has been partially funded by a predoctoral contract (PREDOC20-073), by the

556 Universidad Rey Juan Carlos and project PID2022-139527OB-I00 funded by

557 MCIN/AEI/10.13039/501100011033/ and FEDER.

558

8. References

560 Alonso, J. L., Pulgar, J. A., García-Ramos, J. C., & Barba, P.: Tertiary basins and Alpine tectonics in the
561   Cantabrian Mountains (NW Spain). in Tertiary Basins of Spain (pp. 214–227). Cambridge
562   University Press, 1996
563 Aki, K.: Geometric features of a fault zone related to the nucleation and termination of an earthquake
564   rupture, in: Proceedings of Conference XLV Fault Segmentation and Controls of Rupture Initiation
565   and Termination. US Geological Survey Open File Report 89-315, pp. 1–9, 1989
566 Anderson, E. M: The Dynamics of faulting and Dyke Formation with Applications to Britain (2nd edition),
567   Oliver and Boyd, Edinburgh, Scotland, 1951.
568 Antonellini, M.A., Aydin, A., Pollard, D.D.: Microstructure of deformation bands in porous sandstones at
569   Arches National Park, Utah. J. Struct. Geol., 16, 941e959, 1994.
570 Aydin, A., Nur, A.: Evolution of pull-apart basins and their scale independence. Tectonics 1, 91–105, 1982.
571 Aydin, A.: Fractures, faults, and hydrocarbon entrapment, migration and flow. Mar. Pet. Geol., 17, 797–
572   814, 2000.
573 Aydin, A., & Berryman, J. G: Analysis of the growth of strike-slip faults using effective medium theory. J.
574   Struct. Geol., 32(11), 1629–1642. https://doi.org/10.1016/j.jsg.2009.11.007, 2010.
575 Barka, A., Kadinsky-Cade, K.: Strike-slip fault geometry in Turkey and its influence on earthquake activity.
576   Tectonics, 7, 663–684, 1988.
577 Bartlett, W.L., Friedman, M., Logan, J.M: Experimental folding and faulting of rocks under confining
578   pressure Part IX. Wrench faults in limestone layers. Tectonophysics, 79, 255–277.
579   https://doi.org/10.1016/0040-1951(81)90116-5, 1988.
580 Bullock, R. J., De Paola, N., Holdsworth, R. E., & Trabucho-Alexandre, J.: Lithological controls on the
581   deformation mechanisms operating within carbonate-hosted faults during the seismic cycle. J.
582   Struct. Geol., 58, 22–42. https://doi.org/10.1016/j.jsg.2013.10.008, 2014.

Burgmann, R., Pollard, D.D.: Strain accommodation about strike-slip fault discontinuities in granitic rock under brittle-to-ductile conditions. J. Struct. Geol., 16, 1655–1674, 1994.

Byerlee, J.: Friction of rocks, pages 615–626. Springer, 1978.

Cazarin, C.L., van der Velde, R., Santos, R.V., Reijmer, J.J.G., Bezerra, F.H.R., Bertotti, G., La Bruna, V., Silva, D.C.C., de Castro, D.L., Srivastava, N.K., Barbosa, P. F.: Hydrothermal activity along a strike-slip fault zone and host units in the S˜ao Francisco Craton, Brazil – implications for fluid flow in sedimentary basins. Precambrian Res. 365 https://doi.org/10.1016/j.precamres.2021.106365, 2021.

Cheng, X., Ding, W., Pan, L., Zou, Y., Li, Y., Yin, Y., & Ding, S.: Geometry and kinematics characteristics of strike-slip fault zone in complex structure area: A case study from the south no. 15 strike-slip fault zone in the Eastern Sichuan Basin, China. Front. Earth Sci., 10. https://doi.org/10.3389/feart.2022.922664, 2022.

Cooke, M. L., Toeneboehn, K., and Hatch, J. L.: Onset of slip partitioning under oblique convergence within scaled physical experiments, Geosphere, 16, 875-889. https ://doi.org/10.1130/GES02179.1, 2020.

de Joussineau, G., & Aydin, A.: Segmentation along strike-slip faults revisited. Pure and Applied Geophys, 166(10–11), 1575–1594. https://doi.org/10.1007/s00024-009-0511-4, 2009.

DeDontney, N., Rice, J. R., & Dmowska, R.: Influence of material contrast on fault branching behavior: BIMATERIAL BRANCHING. Geophys. Res. Lett., 38(14). https://doi.org/10.1029/2011gl047849, 2011.

Deng, Q., Wu, D., Zhang, P., & Chen, S.: Structure and deformational character of strike-slip fault zones. Pure and Applied Geophysics, 124(1–2), 203–223. https://doi.org/10.1007/bf00875726, 1986.

Dooley, T. P., & Schreurs, G. : Analogue modelling of intraplate strike-slip tectonics: A review and new experimental results. Tectonophysics, 574–575, 1–71. https://doi.org/10.1016/j.tecto.2012.05.030, 2012

Du, Y., & Aydin, A.: Shear fracture patterns and connectivity at geometric complexities along strike-slip faults. J. Geophys. Res., 100(B9), 18093–18102. https://doi.org/10.1029/95jb01574, 1995.

Fernández, M., Marzán, I., & Torne, M.: Lithospheric transition from the Variscan Iberian Massif to the Jurassic oceanic crust of the Central Atlantic. Tectonophysics, 386(1–2), 97–115. https://doi.org/10.1016/j.tecto.2004.05.005. 2004

Gabrielsen, R. H., Giannenas, P. A., Sokoutis, D., Willingshofer, E., Hassaan, M., & Faleide, J. I.: Analogue experiments on releasing and restraining bends and their application to the study of the Barents Shear Margin. Solid Earth, 14(9), 961–983. https://doi.org/10.5194/se-14-961-2023, 2023

Gamond, J.F.: Displacement features associated with fault zones: a comparison between observed examples and experimental models. J. Struct. Geol., 5, 33–45, 1983.

Gapais, D., Fiquet, G., & Cobbold, P. R.: Slip system domains, 3. New insights in fault kinematics from plane-strain sandbox experiments. Tectonophysics, 188(1–2), 143–157. https://doi.org/10.1016/0040-1951(91)90320-r, 1991.

Gomes, A. S., Rosas, F. M., Duarte, J. C., Schellart, W. P., Almeida, J., Tomás, R., & Strak, V.: Analogue modelling of brittle shear zone propagation across upper crustal morpho-rheological heterogeneities. J. Struct. Geol., 126, 175–197. https://doi.org/10.1016/j.jsg.2019.06.004, 2019.

Harris, R.A., Day, S.M.: Dynamic 3D simulation of earthquakes on en echelon faults. Geophys. Res. Lett., 26, 2089–2092, 1999.

Hatem, A. E., Cooke, M. L., & Toeneboehn, K.: Strain localization and evolving kinematic efficiency of initiating strike-slip faults within wet kaolin experiments. J. Struct. Geol., 101, 96–108. https://doi.org/10.1016/j.jsg.2017.06.011, 2017.

Hatem, A. E., Cooke, M. L., & Toeneboehn, K.: Strain localization and evolving kinematic efficiency of initiating strike-slip faults within wet kaolin experiments. J. Struct. Geol., 101, 96–108. https://doi.org/10.1016/j.jsg.2017.06.011, 2017.

Kim, Y., Peacock, D.C.P., Sanderson, D.J.: Fault damage zones. J. Struct. Geol., 26, 503–517, 2004.

Kirkland, C. L., Alsop, G. I., & Prave, A. R.: The brittle evolution of a major strike-slip fault associated with granite emplacement: a case study of the Leannan Fault, NW Ireland. J. Geol. Soc., 165(1), 341–352. https://doi.org/10.1144/0016-76492007-064, 2008.

Lefevre, M., Souloumiac, P., Cubas, N., & Klinger, Y. : Experimental evidence for crustal control over seismic fault segmentation. Geology, 48(8), 844–848. https://doi.org/10.1130/g47115.1, 2020.

Mair, K., Frye, K.M., Marone, C.: Influence of grain characteristics on the friction of granular shear zones. J. Geophys. Res., 107 (B10), 4/1-4/9, 2002.

Martel, S.J., Peterson Jr., J.E.: Interdisciplinary characterization of fracture systems at the US/BK site, Grimsel Laboratory, Switzerland. International Journal of Rock Mechanics and Mining Science and Geomechanical Abstracts 28, 259–323, 1991.

Martínez Catalán, J. R., Arenas, R., Díaz García, F., & Abati, J.: Variscan accretionary complex of northwest Iberia: Terrane correlation and succession of tectonothermal events. Geology, 25(12), 1103. https://doi.org/10.1130/0091-7613(1997)025<1103:vaconi>2.3.co;2. 1997

Martínez Catalán, J.R. : The Central Iberian arc, an orocline centered in the Iberian Massif and some implications for the Variscan belt. Int. J. Earth Sci. 101, 1299–1314. https://doi.org/10.1007/s00531-011-0715-6, 2012.

Martín-González, F., Heredia, N.: Geometry, structures and evolution of the western termination of the Alpine-Pyrenean Orogen reliefs (NW Iberian Peninsula). J. Iber. Geol. 37, 103–120. https://doi.org/10.5209/rev_JIGE.2011.v37.n2.1, 2011.

Martín-González, F., Barbero, L., Capote, R., Heredia, N., & Gallastegui, G.: Interaction of two successive Alpine deformation fronts: constraints from low-temperature thermochronology and structural mapping (NW Iberian Peninsula). Int. J. Earth. Sci., 101(5), 1331–1342. https://doi.org/10.1007/s00531-011-0712-9. 2012.

Matte, P.: Accretionary history and crustal evolution of the Variscan belt in Western Europe. Tectonophysics, 196(3–4), 309–337. https://doi.org/10.1016/0040-1951(91)90328-p, 1991.

Misra, S., Mandal, N., Chakraborty, C: Formation of Riedel shear fractures in granular materials: Findings from analogue shear experiments and theoretical analyses. Tectonophysics 471, 253–259. https://doi.org/10.1016/j. tecto.2009.02.017. 2009

Moore, J. D. P., & Parsons, B.: Scaling of viscous shear zones with depth-dependent viscosity and power-law stress–strain-rate dependence. Geophys. J. Int., 202(1), 242–260. https://doi.org/10.1093/gji/ggv143, 2015.

Myers, R., Aydin, A.: The evolution of faults formed by shearing across joint zones in sandstone. J. Struct. Geol., 26, 947–966, 2004.

Nicholson, C., Seeber, L., Williams, P. and Sykes, L.R.: Seismic evidence for conjugate slip and block rotation within the San Andreas fault system, Southern California. Tectonics, 5: 629-648, 1986

Odling, N.E., Harris, S.D., Knipe, R.J.: Permeability scaling properties of fault damage zones in siliclastic rocks. J. Struct. Geol., 26, 1727–1747, 2004.

Panien, M., Schreurs, G., & Pfiffner, A.: Mechanical behaviour of granular materials used in analogue modelling: insights from grain characterisation, ring-shear tests and analogue experiments. J. Struct. Geol., 28(9), 1710–1724. https://doi.org/10.1016/j.jsg.2006.05.004, 2006.

Peacock, D.C.P., Sanderson, D.J.: Displacement, segment linkage and relay ramps in normal fault zones. J. Struct. Geol., 13, 721–733, 1991.

Peacock, D. C. P., & Sanderson, D. J.: Effects of layering and anisotropy on fault geometry. J. Geol. Soc., 149(5), 793–802. https://doi.org/10.1144/gsjgs.149.5.0793, 1992.

Petersen, M. D., Dawson, T. E., Chen, R., Cao, T., Wills, C. J., Schwartz, D. P., & Frankel, A. D.: Fault displacement hazard for strike-slip faults. BSSA., 805–825. https://doi.org/10.1785/0120100035, 2011.

Preuss, S., Herrendörfer, R., Gerya, T., Ampuero, J.-P., & Dinther, Y.: Seismic and aseismic fault growth lead to different fault orientations. J. Geophys. Res. Solid Earth., 124(8), 8867–8889. https://doi.org/10.1029/2019jb017324, 2019.

Ramberg, H.: Gravity, deformation and the Earth's crust: In theory, experiments and geological application (p. 452). Academic Press, 1981.

Richard, P.: Experiments on faulting in a two-layered cover sequence overlying a reactivated basement fault with oblique-slip. J. Struct. Geol. 13, 459–469, 1991.

Richard, P., Naylor, M.A., Koopman, A.: Experimental models of strike-slip tectonics. Pet. Geosci., 1, 71–80, 1995.

Riedel, W.: Zur Mechanik geologischer Brucherscheinungen. Centralblatt. 1929.

Rispoli, R.: Stress fields about strike-slip faults inferred from stylolites and tension gashes. Tectonophysics 75, 729–736, 1981.

Ron, H., Freund, R., Garfunkel, Z. and Nur, A.: Block rotation by strike slip faulting: structural and paleomagnetic evidence. J. Geophys. Res., 89: 6256-6270, 1984.

Sammis, C. G., G. King, and R. Biegel, The kinematics of gouge deformation, Pure Appl. Geophys., 125, 777 – 812, 1987.

Schmid, T., Schreurs, G. Warsitzka, M., & Rosenau, M.: Effect of sieving height on density and friction of brittle analogue material: Ring-shear test data of quartz sand used for analogue experiments in the Tectonic Modelling Lab of the University of Bern. GFZ Data Services. https://doi.org/10.5880/fidgeo.2020.006, 2020.

Scholz, C. H.: The Mechanics of Earthquakes and Faulting. Cambridge University Press, 2002.

Schreurs, G.: Experiments on strike-slip faulting and block rotation. Geology, 22(6), 567. https://doi.org/10.1130/0091-7613(1994)022<0567:eossfa>2.3.co;2, 1994.

Schreurs, G.: Structural analysis of the Schams nappes and adjacent tectonic units in the Penninic zone (Grisons, SE-Switzerland). ETH Zurich, 1991.

Schreurs, G.: Fault development and interaction in distributed strike-slip shear zones: an experimental approach. In: Storti, F., Holdsworth, R.E., Salvini, F. (Eds.), Intraplate Strike-slip Deformation Belts. Geol. Soc. Spec. Publ., 210, 35–52, 2003

Shaw, B.E., Dieterich, J.H.: Probabilities for jumping fault segment stepovers. Geophys. Res. Lett., 34, L01307. doi:10.1029/2006GL027980, 2007.

Sibson, R.H.: Stopping of earthquake ruptures at dilational fault jogs. Nature 316, 248–251, 1985.

Stirling, M.W., Wesnousky, S.G., Shimazaki, K.: Fault trace complexity, cumulative slip, and the shape of the magnitude-frequency distribution for strike-slip faults: a global survey. Geophys. J. Int., 124, 833–868, 1996.

Sylvester, A.G.: Strike-slip faults. Geol. Soc. Am. Bull. 100, 1666–1703. https:// doi.org/10.1130/0016-7606(1988)1002.3.CO;2, 1988.

Vegas, R., Vicente Muñoz, G., Muñoz Martín, A., & Palomino, R..: Los corredores de fallas de Régua-Verin y Vilariça: Zonas de transferencia de la deformación intraplaca en la Península Ibérica. 2004

Veludo, I., Dias, N. A., Fonseca, P. E., Matias, L., Carrilho, F., Haberland, C., & Villaseñor, A.: Crustal seismic structure beneath Portugal and southern Galicia (Western Iberia) and the role of Variscan inheritance. Tectonophysics, 717, 645–664. https://doi.org/10.1016/j.tecto.2017.08.018. 2017

Venâncio, M. B., & da Silva, F. C. A.: Structures evolution along strike-slip fault zones: The role of rheology revealed by PIV analysis of analog modeling. Tectonophysics, 229764, 229764. https://doi.org/10.1016/j.tecto.2023.229764, 2023.

Vergés, J., Kullberg, J. C., Casas-Sainz, A., de Vicente, G., Duarte, L. V., Fernàndez, M., Gómez, J. J., Gómez-Pugnaire, M. T., Jabaloy Sánchez, A., López-Gómez, J., Macchiavelli, C., Martín-Algarra, A., Martín-Chivelet, J., Muñoz, J. A., Quesada, C., Terrinha, P., Torné, M., & Vegas, R.: An introduction to the alpine cycle in Iberia. En The Geology of Iberia: A Geodynamic Approach (pp. 1–14). Springer International Publishing. 2019

Visage, S., Souloumiac, P., Cubas, N., Maillot, B., Antoine, S., Delorme, A., & Klinger, Y.: Evolution of the off-fault deformation of strike-slip faults in a sand-box experiment. Tectonophysics, 847(229704), 229704. https://doi.org/10.1016/j.tecto.2023.229704, 2023.

Wesnousky, S.G.: Seismological and structural evolution of strike-slip faults. Nature 335, 340–342, 1988.

Wesnousky, S.G.: Predicting the endpoints of earthquake ruptures. Nature 444, 358–360, 2006.

Westerweel, J., Scarano, F.: Universal outlier detection for PIV data. Experiments in fluids 39, 1096-1100, 2005.

Zhang, X., & Sagiya, T.: Shear strain concentration mechanism in the lower crust below an intraplate strike-slip fault based on rheological laws of rocks. EPS, 69(1). https://doi.org/10.1186/s40623-017-0668-5, 2017.

Zwaan, F., Schreurs, G., Ritter, M., Santimano, T., & Rosenau, M.: Rheology of PDMS-corundum sand mixtures from the Tectonic Modelling Lab of the University of Bern (CH). V. 1. GFZ data Services. https://doi. org/10.5880/fdgeo.2018.023, 2018.